



# Novel hierarchical ferric phosphate/bismuth vanadate nanocactus for highly efficient and stable solar water splitting

Truong-Giang Vo<sup>a,b</sup>, Yian Tai<sup>a,\*</sup>, Chia-Ying Chiang<sup>b,\*</sup>

<sup>a</sup> Nanohybrid Materials and Devices Lab, Department of Chemical Engineering, National Taiwan University of Science and Technology, Taipei, 106, Taiwan

<sup>b</sup> Sustainable Engineering Lab, Department of Chemical Engineering, National Taiwan University of Science and Technology, Taipei, 106, Taiwan

## ARTICLE INFO

### Keywords:

Bismuth vanadate  
Co-catalysts  
Oxygen evolution  
Solar water splitting

## ABSTRACT

Severe surface charge recombination is known as a major energy loss that hinders the performance and durability of solar water splitting. Here, a facile process is developed for preparing a new type of low-cost ferrite phosphate as an efficient co-catalyst to suppress charge recombination and stabilize bismuth vanadate (BiVO<sub>4</sub>) photoelectrodes. The composite photoanode exhibits a high photocurrent density of 2.28 mAcm<sup>-2</sup>, which corresponds to a 250% increase compared to that of pristine BiVO<sub>4</sub>. Deposition of cocatalyst has yielded a large cathodic shift (~500 mV) in the onset potential, high hole oxidation efficiency of about 90%. The Fe-Pi/BiVO<sub>4</sub> photoanode demonstrates an impressive performance of photostability and attains a stable photocurrent density for more than 2 h at 1.23 V<sub>RHE</sub> without declining. Comprehensive photoelectrochemical studies suggest that ferrite phosphate could boost the photoelectrochemical properties of the BiVO<sub>4</sub> underlayer by mediating hole extraction across the photoexcited semiconductor-electrolyte interface. This in turn enhances photoconversion efficiency and prevents the photooxidation of the photoanode, ensuring prolonged stability. The results provide deeper understanding of the role of cocatalyst nanostructures decorated with semiconductors in solar water splitting.

## 1. Introduction

With the increase in serious environment problems, the ever-increasing shortage of energy supply and the rapid demands for renewable energy worldwide in recent decades, photoelectrochemical (PEC) water splitting is now being considered as one of the appealing and highly feasible approaches for converting solar energy directly into the highly-efficient, eco-friendly and sustainable hydrogen energy [1]. However, harvesting light to split water presents thermodynamic and kinetic challenges, with major efficiency losses associated with oxygen production [2]. Furthermore, electrode material stability is often poor under the harsh conditions in which this reaction occurs. Therefore, significant attention has been devoted to the development of *n*-semiconductors that are chemically stable and harvest sunlight and can oxidize water efficiently. Among the available candidates for photoanodes, bismuth vanadate is a promising one. It has garnered significant interest because of its 2.4 eV band gap, relatively long photo-carrier lifetimes [3] and has favorable band alignment for water oxidation [4]. However, the effective photoelectrochemical (PEC) water oxidation performance of bismuth vanadate still fails to reach the theoretical values which are approximately 6.2–7.5 mAcm<sup>-2</sup> because

of its sluggish water oxidation kinetics and poor carrier transport [5–8]. Numerous efforts have been implemented to overcome these deficiencies, such as elemental doping (e.g., Mo, W) to improve the electronic conductivity and facilitate the charge transfer [9–12], structure controlling, heterojunction, and passivating the surface states by surface deposition of the metal oxides overlayer [13]. Nevertheless, these approaches predominantly focus on the intrinsic charge separation and transport of BiVO<sub>4</sub>, while the sluggish oxygen evolution reaction (OER) at the solid/liquid interfaces cannot be effectively resolved through the above-mentioned strategies.

Recently, the coupling of a water oxidation co-catalyst (WOC) with metal oxides semiconductors has been proved to be an effective strategy for promoting solar water oxidation by minimizing the kinetic overpotential and providing active sites for water oxidation [14,15]. More importantly, given the rapid transfer of the remaining holes in the semiconductor to water oxidation catalysts after photoelectrochemical charge separation when a co-catalyst is employed, photostability is also greatly enhanced. Consequently, there is a substantial need for developing WOCs that could be readily deposited with high catalytic activity and stability to break the chain of the inferior PEC water oxidation performances. Although numerous 3d metal-based WOCs have been

\* Corresponding authors.

E-mail addresses: [ytai@mail.ntust.edu.tw](mailto:ytai@mail.ntust.edu.tw) (Y. Tai), [cychiang@mail.ntust.edu.tw](mailto:cychiang@mail.ntust.edu.tw) (C.-Y. Chiang).

<https://doi.org/10.1016/j.apcatb.2018.11.001>

Received 8 September 2018; Received in revised form 29 October 2018; Accepted 1 November 2018

Available online 03 November 2018

0926-3373/© 2018 Elsevier B.V. All rights reserved.

widely researched for water splitting [16–21], only appropriate cases have been successfully implanted into PEC water oxidation reactions under simulated sunlight for various reasons, including different deposition methods and complicated WOC/semiconductor interfaces. Consequently,  $\text{CoP}_i$  [22,23],  $\text{Ni-Bi}$  [24],  $\text{FeO}_x$  [21],  $\text{NiCoO}_x$  [25], and  $\text{FeOOH}$  [15], were integrated with bismuth vanadate photoanode to improve surface kinetics, thus facilitating the PEC water oxidation activity.

More recently, transition-metal phosphates have been reported to exhibit higher oxygen evolution reaction (OER) activity. The presence of phosphate groups in  $\text{Ni-Pi}$  [26] and  $\text{Co-Pi}$  has been demonstrated to play an important role in facilitating the adsorption, and thus the oxidation, of water. For example, Hamann et al. found that  $\text{Co-Pi}$  catalysts can efficiently collect and store photogenerated holes from the hematite electrode, which contributes to the reduced surface state recombination and increases water oxidation efficiency [27]. Jin and colleagues concluded that the phosphate groups in  $\text{Mn}_3(\text{PO}_4)_2$  stabilize  $\text{Mn(III)}$ , thereby facilitating the oxidation of water [28]. Zhan et al. also showed that nickel phosphate, in which the catalytic centers are stabilized by the phosphate framework, has better OER activity than other  $\text{Ni}$ -based OER catalysts. More importantly, it is reported that morphological structures have a critical effect on the electrochemical properties of metal phosphates [29–32]. For example, metal-based phosphate with various peculiar morphologies such as nanowire [30] and nanocluster [29] have been fabricated for OER electrocatalyst. Nevertheless, studies into their morphology with a uniquely stacked nanosheet, which highly facilitates the photosynthetic reaction area, are rare.

With these regards in mind, in this work, we report a facile and rapid strategy for directly integrating a ferric phosphate (denotes as  $\text{Fe-Pi}$ ) nanosheet on  $\text{BiVO}_4$  photoanode in ambient conditions without using a binder or post-synthetic treatment. It is found that the introduction of  $\text{Fe-Pi}$  offers a considerable support to efficient hole transfer and consumption against the unproductive and energy-wasted surface charge recombination, thus resulting in a reduction in surface kinetics barriers and lowering of the water oxidation onset potential. Furthermore, it is demonstrated that phosphate anions in the  $\text{Fe-Pi}$  nanosheet could also have a synergistic effect on promoting the multiphoton-coupled electron transfer process for the PEC water oxidation and can function as effective linkers between  $\text{BiVO}_4$  and iron cations in the  $\text{Fe-Pi}$  nanosheet. This is responsible for the enhanced activity for PEC water oxidation of the modified  $\text{BiVO}_4$  film under solar irradiation and its activity stability. This work would provide feasible routes for the design and synthesis of high-performance bismuth vanadate-based PEC nanomaterials for water splitting.

## 2. Experimental

### 2.1. Preparation of $\text{Fe-Pi/BiVO}_4$ photoanodes

$\text{BiVO}_4$  photoanodes were fabricated on the basis of the method reported in a recent study with a few modifications as briefly described in Fig. 1 (details available in the Supporting Information (SI)). [33,34]. Iron-phosphate ( $\text{Fe-Pi}$ ) deposition is mainly based on the adsorption and reaction mechanism of the ions from the cationic and anionic solution, respectively, by a two-step successive ionic layer adsorption and reaction (SILAR) method. The as-obtained  $\text{BiVO}_4$  (noted as  $\text{BVO}$ ) substrate was immersed in 25 mM  $\text{KH}_2\text{PO}_4$  solution (100 mL) for 30 s. After that, the substrate was immersed in 25 mM  $\text{FeCl}_3$  aqueous solution (100 mL) for another 30 s. The process was repeated 20 times to obtain an optimum loading amount. The substrate was rinsed in deionized water after every 5 cycles to avoid particle aggregation that could lead to inhomogeneous growth of  $\text{Fe-Pi}$ . Finally,  $\text{Fe-Pi}$  decorated  $\text{BVO}$  film was washed with deionized water to fully clean up the loosely bonded particles and then dried at ambient condition prior to use.

For comparison and mechanistic study purpose, various modified  $\text{BVO}$  electrodes including iron (III) ion or phosphate ion absorption

were prepared and denoted as  $\text{Fe}^{3+}/\text{BVO}$ ,  $\text{PO}_4^{3-}/\text{BVO}$ , respectively (details available in SI).

### 2.2. Material characterization

The crystal structure was investigated by X-ray diffractometer (XRD,  $\text{Cu K}\alpha$  radiation, Bruker D2 Advance) and Raman spectrometer (Jasco NRS-5100, 532 nm excitation laser). The morphology and composition analyses were conducted by field emission scanning electron microscope (FE-SEM, JEOL JSM-6700) with an accelerating voltage of 15 kV combined with an energy dispersive spectroscopy (EDS). The chemical composition for these photoanodes was studied by X-ray photoelectron spectroscopy (XPS, Thermo VG ESCALAB250). Optical characteristic was recorded by Ultraviolet-visible spectrometer (UV-vis, Jasco V650) equipped with an integrated sphere using  $\text{BaSO}_4$  as a background. Fourier-transform infrared spectroscopy (FTIR) was obtained by Bio-Rad FTS 3500 spectrometer under attenuated total reflection (ATR) conditions. The data were recorded in the 400–4000  $\text{cm}^{-1}$  range.

### 2.3. Photoelectrochemical characterization

All PEC measurements were conducted by using a three-electrode system, in which as-prepared photoanode,  $\text{Ag/AgCl}$  (3 M  $\text{KCl}$ ) and  $\text{Pt}$  mesh (2.5 cm  $\times$  2.5 cm) served as the working electrode, reference electrode, and counter electrode, respectively. The light source was a 500 W Xe lamp (Model 66905, Newport) coupled with an AM 1.5 G filter. The electrochemical quartz cell was placed at an appropriate position to achieve power density of 100  $\text{mWcm}^{-2}$  at the electrolyte/electrode interface as measured by a Newport thermopile detector. Unless stated otherwise, the light was perpendicularly irradiated through the substrate side (back-side). Measurements were conducted and monitored by a potentiostat (Autolab PGSTAT302N, Netherlands). A 0.1 M  $\text{Na}_2\text{B}_4\text{O}_7$  aqueous solution (pH 9.4), referred to as  $\text{NaBi}$  solution hereafter, was used as the electrolyte. J-V curves of the samples were performed at scan rates of 20 mV/s. Unless otherwise specified, all the potentials were referred to reversible hydrogen electrode.

J-V plots in 0.1 M  $\text{NaBi}$  solution containing 0.1 M  $\text{Na}_2\text{SO}_3$  as a hole scavenger were recorded to determine the charge separation efficiency in the bulk ( $\eta_{\text{bulk}}$ ) and on the surface ( $\eta_{\text{surface}}$ ).

Chopped-light amperometric J-t measurements were performed at an applied potential of 1.23 V under chopped light irradiation (light on or off cycles: 10 s). The long-term stability photoanodes for oxygen evolution reaction was evaluated by chronoamperometry with a controlled potential at +1.23 V for several hours. The solution was gently stirred to circulate the electrolyte and remove bubbles from the film surface.

The electrochemical impedance spectroscopy (EIS) measurement was done over a frequency range of  $10^5$ –0.1 Hz and at an amplitude of 10 mV under AM 1.5 G light irradiation (100  $\text{mW/cm}^2$ ). The impedance data measured were fitted to an appropriate equivalent circuit by using Nova software (version 1.11) to derive the resistance values.

The incident-photon to current efficiency (IPCE) spectra were acquired under irradiated condition. The light from a 500 W Xe lamp (Model 66905, Newport) was focused through the monochromator (Oriel Cornerstone 130, Newport) onto the working electrode, and the monochromator was incremented in the spectral range (300–600 nm) with a sampling interval of 10 nm and a current sampling time of 10 s. The light power for each wavelength was measured by an optical power meter (Model 843R, Newport).

## 3. Results and discussion

### 3.1. Phase structure and morphology

The bismuth oxyiodide ( $\text{BiOI}$ ) nanosheet template on FTO was first prepared by a simple electrodeposition (Fig. 1) and then converted to

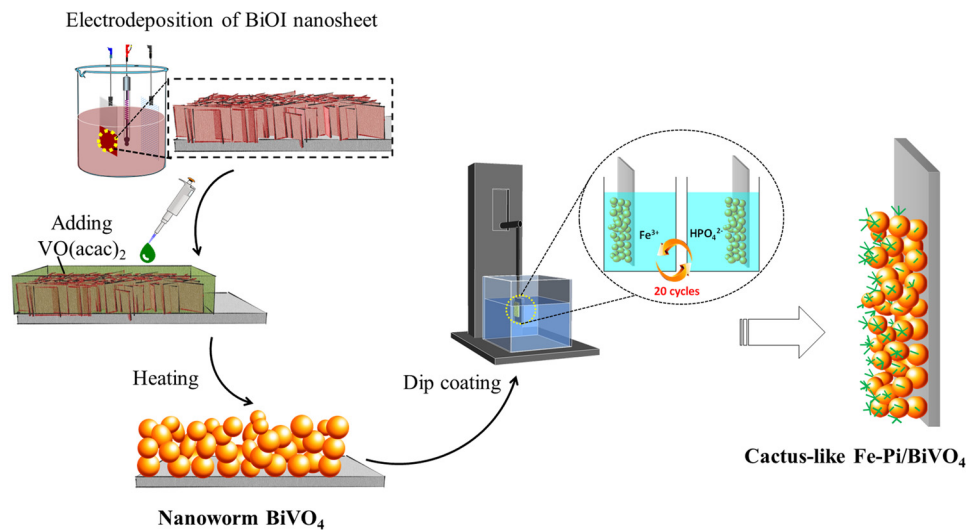


Fig. 1. Schematic illustration of the fabrication process of Fe-Pi/BVO photoanode.

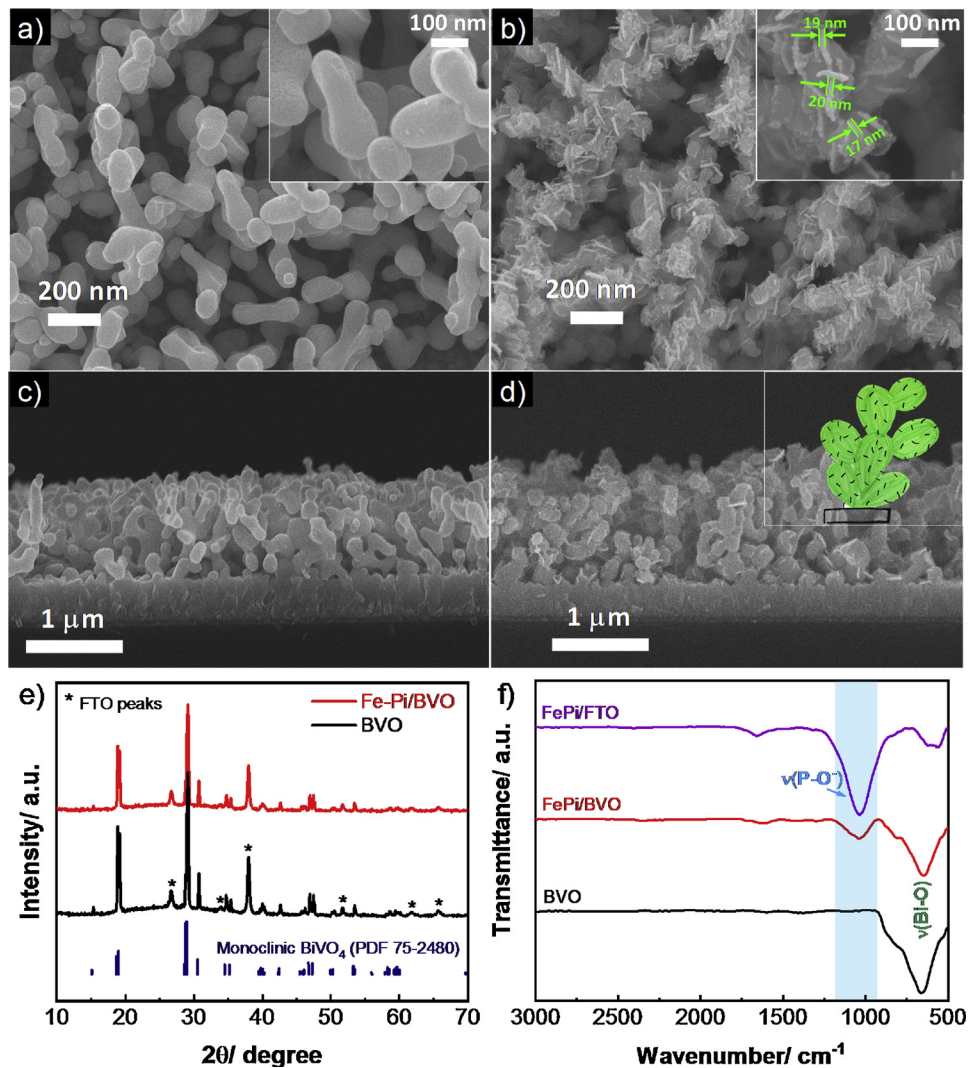


Fig. 2. Top-view scanning electron microscopy (SEM) image of BVO (a, c) and Fe-Pi/BVO (b, d); X-ray diffractogram (e) and ATR-FTIR spectra of BVO before and after decorating with iron phosphate (f). Inset in panel (d) shows the image of a cactus with the similar hierarchical morphology.

BVO by intercalation of vanadium. As shown in Fig. S1, BiOI possessed a two-dimensional architecture, which consisted of a small and ultrathin plate (ca. 18 nm in thickness and 1.2  $\mu\text{m}$  in height) with sufficient voids for large grain growth of  $\text{BiVO}_4$  particles during the calcination process. After calcination, it is found that the BVO film exhibited wormlike-shaped particles with average diameter of 100–200 nm (Fig. 2a), forming a three-dimensional (3D) nanoporous structure. Fe-Pi was further deposited grown on the BVO surface and it covered BVO with evenly-distributed ultrasmall sheet-like crystals, generating cactus-like Fe-Pi/BVO photoanodes (Fig. 2b). The elemental composition of Fe-Pi/BVO was determined and illustrated in Fig. S2, which provided evidence for the existence of Fe and P on the BVO electrode.

The phase and crystal structure of BVO and Fe-Pi were examined by XRD (Fig. 2e). Several diffraction peaks corresponding to  $\text{SnO}_2$  (JCPDS 41-1445) could be observed in both of the samples that were derived from the FTO substrate. The pattern of pristine BVO matched well with the standard monoclinic bismuth vanadate (JCPDS 75-2480), suggesting that there was a complete transformation of bismuth oxyiodine to bismuth vanadate after calcination. In terms of Fe-Pi/BVO, no characteristic diffraction peaks of Fe-Pi could be observed, indicating that Fe-Pi was not in the highly crystalline state. The amorphous state of Fe-Pi co-catalyst could also be verified by its powder XRD pattern (Fig. S3). This was in accordance with the result reported for the Fe-Pi deposition on nickel foam substrate [35]. ATR-FTIR spectroscopy experiments confirmed that Fe-Pi was successfully attached to BVO. As can be seen in Fig. 2f, the characteristic band at about  $570\text{--}600\text{ cm}^{-1}$  corresponds to the vibration of metal-oxygen, while the new IR bands at about  $1035\text{ cm}^{-1}$  can be attributed to O-P-O deformation that strongly bound to BVO surface [36–38]. This finding presents the proof for structural confirmation of ferric phosphate. Additionally, the Raman spectra of BVO, Fe-Pi/BVO and a reference Fe-Pi powder are presented in Fig. S4. It was found that all the samples showed six bands at about 128, 211, 325, 367, 705 and  $820\text{ cm}^{-1}$  as pure scheelite monoclinic bismuth vanadate, implying that the nanostructure of BVO could be maintained after coupling with Fe-Pi. Neither additional peaks for Fe-Pi nor a significant shift in the peaks' positions were observed after decorating with the Fe-Pi catalyst. Further observation indicated that, after modification with iron phosphate, the peak intensity of BVO decreased to some extent, compared with the pure BVO, owing to the good surrounding of BVO by Fe-Pi.

Further evidence of the retention of Fe-Pi was obtained by X-ray photoelectron spectroscopy (XPS). The survey XPS spectrum, as well as the spectra for the Fe, P and O, are shown in Fig. 3(a). In the Fe 2p core-level spectrum (Fig. 3b), the binding energy of Fe  $2p_{3/2}$  at around 710.8 eV was consistent with the typical value of  $\text{Fe}^{3+}$ . The P 2p spectrum of Fe-Pi/BVO, with the peak centered at around 133.2 eV (Fig. 3c), provided evidence of the existence of metal phosphate. Meanwhile, as can be seen in Fig. 3(d), O 1s spectrum can be decomposed into three peaks. It is probable that the peak at about 530.2 eV was indexed to the binding energy of the metal-oxygen bond and a strong peak at 531.5 eV can also be assigned to the O–P bonding in the phosphate group. Additionally, another peak at 532.6 eV was indicative of oxygen in surface-absorbed oxygen. Thus, taken together, all of the above physicochemical results suggested that nanosheet-stacked Fe-Pi was successfully deposited on BVO through a simple dipping deposition.

In order to understand the effect of Fe-Pi loading on the optical absorption properties of BVO, the UV–vis absorbance spectra for bare BVO and Fe-Pi/BVO films were measured. As shown in Fig. 4a, both spectra show the typical feature of BVO with absorption edges around 500 nm. The band gap of films was calculated on the basis of the UV–vis absorbance spectra, which is shown in the inset of Fig. 4a. Regardless of Fe-Pi decoration, both films had the same band gap of  $\sim 2.48\text{ eV}$ , which was in agreement with the reported band gap of 2.4–2.5 eV for monoclinic bismuth vanadate. Additionally, the BVO and Fe-Pi/BVO films revealed a similar absorbed photon flux (shown in Fig. 4b), and the

total absorbed photocurrent values of BVO and Fe-Pi/BVO films were integrated to be  $4.35\text{ mA cm}^{-2}$  and  $4.11\text{ mA cm}^{-2}$ , respectively.

### 3.2. Photoelectrochemical properties of as-prepared photoanodes

Photocurrent density-potential (J-V) curves of BVO and Fe-Pi/BVO photoanodes were recorded in 0.1 M borate solution (pH 9.4) under intermittently chopped and continuous illumination (Fig. 5a and b). As seen in Fig. 5a, the unmodified BVO exhibited a photocurrent density of  $0.98\text{ mA cm}^{-2}$  at 1.23 V. Upon deposition of the BVO with Fe-Pi, a significantly higher photocurrent density was obtained within the entire range of applied potential. At 1.23 V, the photocurrent density Fe-Pi/BVO reached  $2.28\text{ mA cm}^{-2}$ , which was a 240% improvement over the bare BVO film. In order to eliminate the possibility that Fe-Pi itself was photoactive along with the BVO photoanode, Fe-Pi was deposited on FTO glass and then the J-V curve was recorded. It can be seen in Fig. S5 that there was no observable photocurrent upon illumination of the Fe-Pi electrode. This reflected that Fe-Pi alone was inactive toward photooxidation of water and it merely played a role as WOC on the BVO photoanode.

Apart from the photocurrent values, the photocurrent onset potential ( $V_{\text{on}}$ ) was estimated by using the Butler method [39]. As shown as Fig. 5c, the Fe-Pi/BVO photoanode remarkably lowered the onset voltage of photocurrent generation by ca. 500 mV. This suggested that OER kinetics was improved upon the deposition of Fe-Pi. Given that the adsorption of metal cation onto the surface of photoanode might also enhance the PEC water oxidation efficiency in a manner similar to metal phosphate [40,41],  $\text{Fe}^{3+}$ -impregnated BVO (denoted as  $\text{Fe}^{3+}/\text{BVO}$ ) was also investigated. It is found that adsorption of  $\text{Fe}^{3+}$  ions onto the surface of BVO only showed a slight cathodic shift ( $\sim 100\text{ mV}$ ) in onset potential, illustrating that the improvements in PEC performance of BVO photoanode obtained using Fe-Pi rather than surface-adsorbed  $\text{Fe}^{3+}$  as the electrocatalyst. In the meantime, no obvious shift of the onset potential was observed for phosphate-modified BVO (Fig. 5b) suggesting that the phosphate anion itself did not accelerate the water oxidation kinetics and iron was the primary active site for OER. However, this did not mean that the phosphate ion played no role in the enhancement of the current densities. The presence of phosphate ion might provide favorable charge transport in the photoanode which will be discussed in detail in the later section.

In addition to the increased photocurrent and reduced  $V_{\text{on}}$  in general, it is interesting to note that the promotional effect was more pronounced at the lower potential range than the higher potential region. Specifically, the photocurrent of Fe-Pi/BVO experienced a 7-fold increase at the potential as low as 0.7 V. Hence, to quantitatively evaluate the efficiency of PEC water splitting of the photoanodes, applied bias photon-to-current efficiency, (ABPE, also known as photo-conversion efficiency) calculated by using its J-V curve assuming 100% faradaic efficiency, was plotted in Fig. 5d. The maximum ABPE of 0.82% was achieved at a potential as low as 0.67 V. This result is superior to the  $\text{RhO}_2/\text{Mo-doped BiVO}_4$  system [42] (0.6% at 0.88 V), and it is also higher than the findings in a similar report by Pilli and coworkers, in which a  $\text{Co-Pi/SiO}_2\text{-BiVO}_4$  electrode exhibited 0.58% ABPE at 0.7 V applied bias [43]. This result suggests that Fe-Pi can suppress charge recombination efficiently, thus enhancing the overall efficiency of solar water splitting.

### 3.3. Evaluation of PEC stability

Given that long-term stability under prolonged illumination in aqueous solution is another essential criteria for the practical application of photoelectrodes, continuous photoelectrolysis was performed at a fixed potential of 1.23 V in 2 h. As can be seen in Fig. 6b, the photocurrent of bare BVO dropped rapidly within only 15 min. Interestingly, the Fe-Pi/BVO photoelectrodes remained stable with only a slight attenuation of 5% in comparison to the initial value under the same PEC



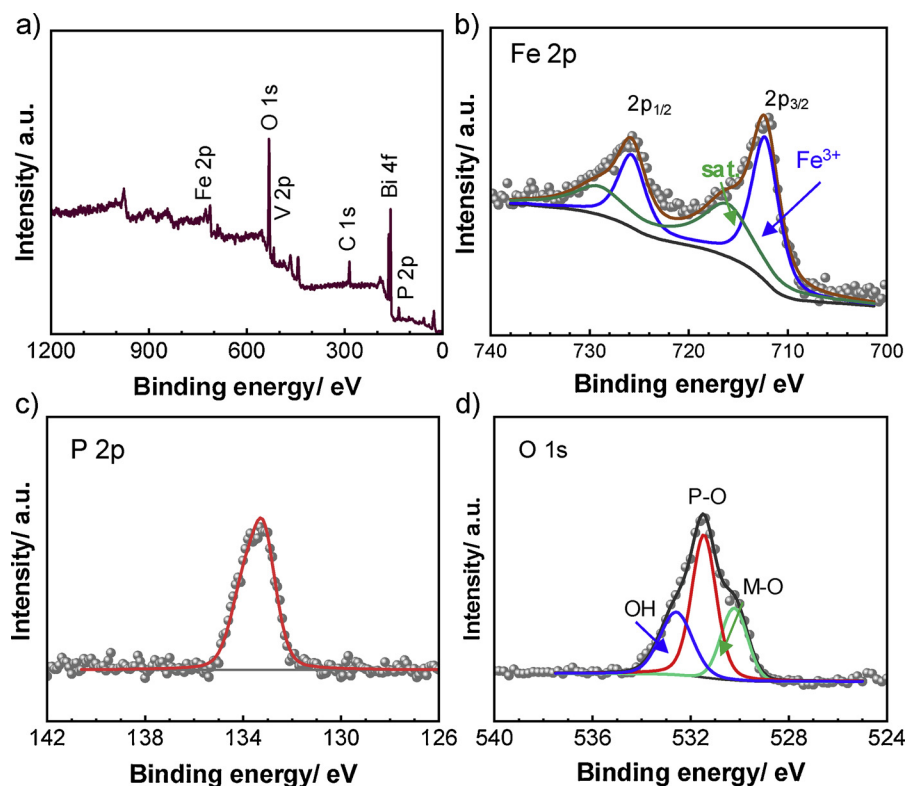


Fig. 3. XPS survey spectrum of Fe-Pi/BVO photoanode (a) and high-resolution XPS for Fe 2p (b), P 2p (c) and O 1s (d).

conditions. Additionally, there was no noticeable change in the morphology of the nanostructures nor the surface composition after 2 h of ongoing operation (Fig. S6 and Fig. S7), as evidenced by SEM and XPS. Moreover, the ICP-AES measurements also showed that no iron residue was detected in the electrolyte solution after 2 h of running OER, further confirming the stability of the Fe-Pi/BVO photoanode (Fig. S8 and Table S1). Considering that an understanding of the factors governing the photoelectrochemical durability of the photoanode may provide the basis for rational photoanode design, significant effort was made to examine the structure, the chemical composition, and surface oxidation states more thoroughly. Although the photocurrent of BVO was observed to decline significantly by more than 50% after J-t testing, the subsequent J-V curve of BVO in the presence of a sacrificial hole acceptor, such as a  $\text{Na}_2\text{SO}_3$ , generated a significant photocurrent (Fig. S9). Moreover, the SEM and XPS of the BVO electrode after 2 h of J-t measurement showed that a considerable amount of BVO still remained on the substrate (Fig. S10 and S11), suggesting that the drastic photocurrent decay during the J-t measurement was not entirely due to the loss of BVO as illustrated in Fig. 6(a). Moreover, when the BVO photoanode was re-assessed in 0.1 M NaBi electrolyte containing 0.2 M sulfite, a stable photocurrent was generated for 2 h without any sign of observable decay (Fig. S12). Overall, the authors believe that the majority of the photocurrent degradation of BVO during water oxidation is associated with its poor kinetics for water oxidation, resulting in the severe recombination between and photogenerated electron-hole pairs (Fig. 6b) [34]. Therefore, it is reasonable to confer that if the surface-reaching holes are consumed quickly for the interfacial oxidation reaction and are not accumulated at the surface,  $\text{BiVO}_4$  could be photostable under identical conditions [44]. In this study, the addition of an efficient water oxidation catalyst, such as ferrite phosphate, significantly promoted hole injection efficiency and reduced the competing reaction of surface oxidation of the photogenerated hole itself, thus achieving significantly improved efficiency.

A detailed comparison in performance and stability of WOC loaded  $\text{BiVO}_4$  photoanodes that have recently been reported was tabulated in

**Table 1.** Fe-Pi/BVO exhibits high photocurrent density compared to any other single co-catalyst decorated BVO perhaps owing to its unique hierarchical structure. Although there is no doubt that photoelectrode decoration with a catalyst could bring a huge improvement in the PEC performance as well as the stability, it worths noting that the catalyst performed differently with different preparation processes.

#### 3.4. Mechanistic study on the effect of FePi decoration on PEC performance

Based on the preceding discussion, it can be stated that Fe-Pi decoration on the BVO surface generated notable improvements in photocurrent generation, onset potential, and long-term durability. These results provided motivation for the instigation of a comprehensive investigation on the origins of such an extraordinary enhancement, as well as to gain a deeper understanding of the functionality of the ferrite phosphate catalyst. Thus, the optical, electronic and photoelectrochemical properties of BVO and Fe-Pi/BVO were carefully investigated. Firstly, to confirm whether the light absorption contributed to the enhanced photocurrent densities, their incident photon-to-current conversion efficiency (IPCE) curves were measured at 1.23 V versus RHE under AM 1.5 G illumination (Fig. 7a). The photoresponse of the samples was consistent with the UV-vis spectra (Fig. 4a), which indicated that the photocurrent mainly originated from the band gap transition of BVO, while the Fe-Pi predominantly played the role of co-catalyst. Next, it is important to determine the rate-limiting factor of the Fe-Pi-catalyzed BVO. Photoelectrocatalytic activities were re-assessed in the presence of 0.1 M sodium sulfite, which served as a hole scavenger. As sulfite oxidation was thermodynamically favored and was kinetically facile with respect to water oxidation, this approach enabled the investigation of the photoelectrochemical properties of photoanodes independently of their poor water oxidation kinetics.

Fig. 7(b) shows a typical J-V curve for sulfite oxidation of BVO and Fe-Pi/BVO. A very early photocurrent onset potential and a rapid increase in photocurrent in the range of 0.3 to 0.6 V resulted in an increase in the photocurrent density from 0.98 to  $2.56 \text{ mAcm}^{-2}$  for bare

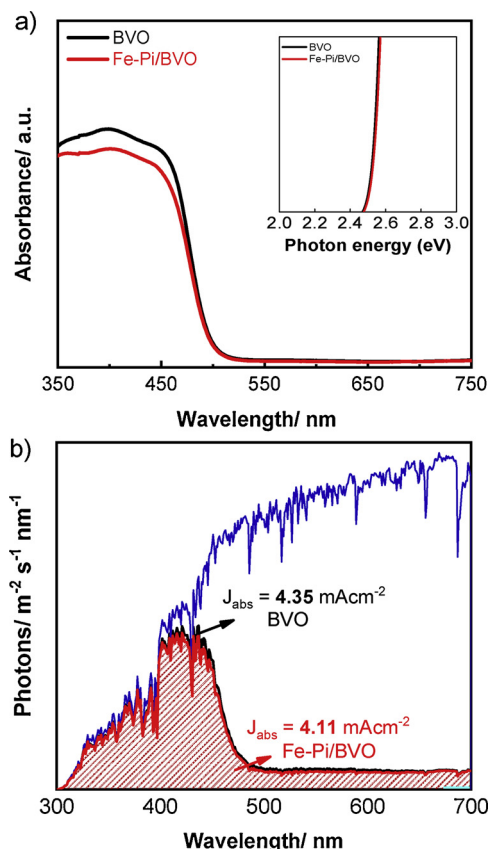


**Fig. 4.** UV-vis absorption spectra and Tauc plot (the inset) of BVO before and after decorating with iron phosphate (a); Photon flux under AM 1.5 G (ASTM G173-03) and those weighted by the absorption spectra of Fe-Pi/BVO (red) and BVO films (black) (b) (For interpretation of the references to colour in this figure legend, the reader is referred to the web version of this article.).

BVO. Photocurrent from the bare BVO for water oxidation was significantly lower than the photocurrent for sulfite oxidation, revealing that the majority of surface-reaching holes were lost to surface recombination. In the meantime, the J-V plot of Fe-Pi/BVO for water oxidation was almost comparable to that of sulfite oxidation, indicating that the presence of Fe-Pi effectively increased the rate of water oxidation and can prevent surface hole accumulation and photocorrosion. For direct comparison, hole injection efficiency ( $\eta_{\text{surface}}$ ), which represents the fraction of the holes that reach the electrode/electrolyte interface and participate in water oxidation, was calculated and plotted in Fig. 7(d) [45,46]. Evidently, the hole injection yield of the BVO photoanode remained below 40%, indicating that more than half of the photogenerated holes were wasted by surface recombination instead of contributing to the water oxidation reaction. However, after the deposition of Fe-Pi, the  $\eta_{\text{surface}}$  started from 60% at 0.5 V, became 80% at 1.2 V and reached 90% above 1.3 V. Apparently, Fe-Pi loading brought nearly complete injection of holes arriving at the surface of the photoanode from its bulk into water oxidation, avoiding loss by surface recombination with electrons. In terms of bulk charge separation ( $\eta_{\text{sep}}$ ) [46,47], as seen in Fig. 7(d), there was no significant difference between BVO and Fe-Pi/BVO, indirectly indicating that Fe-Pi in fact only served to transfer the captured holes to the electrolyte for OER, which means that its influence on charge separation was minimal.

The transient photocurrent responses of bare BVO and Fe-Pi/BVO at a constant bias of 1.23 V for several on-off cycles were recorded to investigate water oxidation dynamics behavior. As shown in Fig. 8(a), the BVO photoanode showed a high spike in the current, indicating the presence of a high injection barrier. Conversely, the photoresponse of the Fe-Pi/BVO was fast and reproducible under chopped illumination

with no observable spikes, implying the efficient charge utilization that resulted from surface modification. To substantiate the deduction, we performed a calculation to analyze the transient decay time using the following equation:

$$D = \frac{I_t - I_s}{I_m - I_s}$$

where  $I_t$  is the current at time  $t$ ,  $I_s$  is the stabilized current, and  $I_m$  is the current spike. The transient decay time can be defined as the time at which  $\ln D = -1$  [48]. Evidently, as can be seen in Fig. 8b, with the coverage of Fe-Pi, the transient decay time became longer than the bare BVO, testifying to the abating of the recombination rate.

The enhancing mechanism of the ultrasmall Fe-Pi nanosheet on the BVO photoanode was further investigated by electrochemical impedance spectroscopy (EIS) at 1.23 V under AM 1.5 G illumination. Under illumination, all electrodes showed a typical semicircle arc with different radii in the measured frequency region (Fig. 8c). Herein, we adopted a simple equivalent circuit, which consisted of electrolyte resistance ( $R_s$ ), charge transfer resistance ( $R_{ct}$ ) of the photoanode/electrolyte interface and a capacitance phase element (CPE). The dramatic reduction in the arc diameter upon the loading of the Fe-Pi nanosheet indicates lower charge-transfer resistance at the electrode/electrolyte interface than that of the bare BVO. In other words, photogenerated holes on Fe-Pi/BVO photoanode can inject into electrolytes more easily than in a pristine BVO photoanode via an alternative pathway for transfer of holes, which prevents hole accumulation at the BVO surface. Since it is known that surface decoration of co-catalysts cannot change the conductivity of the BVO photoanode, EIS analyses confirm that the improved interface charge transfer is one of the dominant reasons for the enhanced PEC performance.

The effect of surface modification on the charge carrier kinetics is more intuitively reflected in the Bode plots of the Fe-Pi/BVO electrodes (Fig. 8d). In terms of the BVO electrode, the low-frequency peak showed a significantly higher phase value, suggesting that water oxidation was limited by charge transfer at the electrode/electrolyte interface [49]. After the loading of the Fe-Pi co-catalysts, the low-frequency peak of BVO decreased and shifted toward the lower frequency. It confirms the longer electron lifetime in the modified BVO sample. This result was consistent with the transient photocurrent decay time plot, which suggested that the recombination of photogenerated carriers has been inhibited by surface modification. Additionally, the slopes of the Mott-Schottky plot (shown in Fig. S13), which correspond to the charge carrier concentration, showed no significant difference between BVO and Fe-Pi/BVO photoanode. Therefore, the possibility of forming a heterojunction between the co-catalyst and the semiconductor which could promote the charge separation and transfer can be eliminated. Similar behavior was also reported for Ni and Co-based catalysts deposited on BVO photoanodes [25].

The proposed mechanism of water oxidation reaction on Fe-Pi/BVO hybrid photoelectrode is illustrated in Fig. 9. Generally, the illumination of BVO produces electron-hole pairs. Electrons in the conduction band were transported to FTO back contact under applied bias and enter the external circuit to participate in the reduction of  $\text{H}_2\text{O}$  at the Pt cathode surface. A certain proportion of the photocurrent density was lost because of the bulk recombination in BVO. Meanwhile, the photogenerated holes must be transported to the semiconductor/electrolyte interface with sufficient efficiency to drive the oxygen evolution reaction at the surface of the photoanode. Regrettably, because of the sluggish kinetics of water oxidation at the BVO surface, hole accumulation near the surface resulted in the recombination between these holes and the electrons of the BVO conduction band. Therefore, in the absence of Fe-Pi, there was a significant kinetic competition between water oxidation and surface recombination and this effectively restricts the PEC performance. In the presence of Fe-Pi, Fe (III) ions could effectively capture photogenerated holes to form high-valence iron ions which would easily induce the water oxidation reactions to evolve  $\text{O}_2$ ,

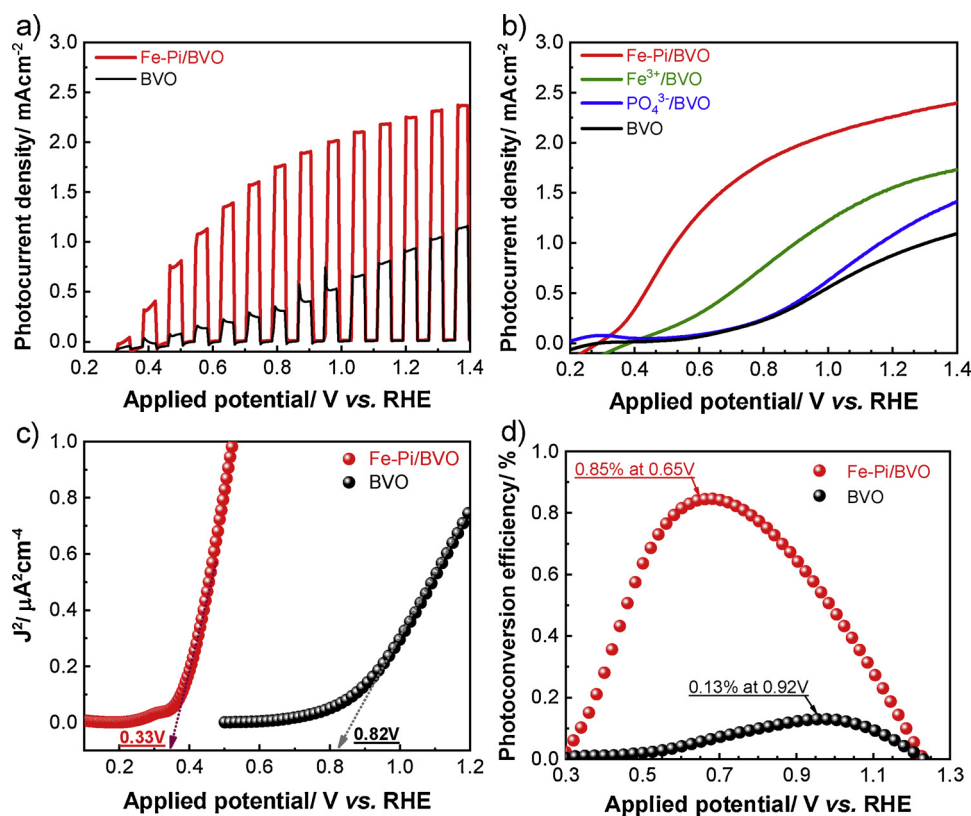


**Fig. 5.** Photocurrent-potential curves of BVO and Fe-Pi/BVO measured under chopped light irradiation (a); Photocurrent density versus applied potential (J-V) curves of BVO, Fe/BVO and, Pi/BVO and Fe-Pi/BVO under continuous illumination (b); corresponding Butler plots, in which the onset potential is defined (c); Applied bias photon-to-current efficiency of BVO and Fe-Pi/BVO derived from their corresponding J-V curves (d). All measurements were taken in 0.1 M NaBi solution.

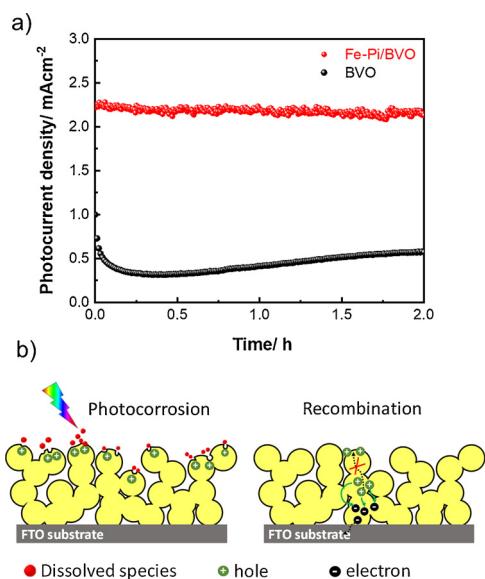


**Fig. 6.** Time-dependent photocurrent density curves of BVO and Fe-Pi/BVO at 1.23 V vs RHE under illumination (a); Schematics of the proposed pathway for photocurrent decay on BVO photoanode (b).

thus surface charge separation was promoted [50–52]. Simultaneously, after reacting with  $H_2O$ , iron species return to their original valence state. While the catalytic role of Fe (III) active centers toward water oxidation is straightforward, it is believed that phosphate groups also played an essential role in the activity-enhanced mechanism of Fe-Pi co-catalyst. Phosphate anions are known to strongly adsorb onto the surfaces of (oxyhydr)oxide materials by substituting surface hydroxyl groups which would effectively facilitate the metal cation connected to the semiconductor surface and provide favorable charge transport in the photoanode [37,53,54]. Additionally, several studies have also

**Table 1**

The PEC performance of OER cocatalyst decorated  $BiVO_4$  photoanode.

Material	Performance (at 1.23 V <sub>RHE</sub> )	Shift in V <sub>OC</sub>	%photocurrent decay	Reference
Fe-Pi/ $BiVO_4$	2.28 mA/cm <sup>2</sup>	490 mV	10% after 6h	This study
Ni-C <sub>60</sub> /W: $BiVO_4$	2.18 mA/cm <sup>2</sup>	371 mV	~20% after 2 h	[57]
FeO <sub>x</sub> / $BiVO_4$	1.1 mA/cm <sup>2</sup>	300 mV	~45% after 1h	[21]
CoO <sub>x</sub> / $BiVO_4$	1.49 mA/cm <sup>2</sup>	400 mV	~10% after 10 min	[18]
NiO <sub>x</sub> / $BiVO_4$	1.18 mA/cm <sup>2</sup>	280 mV	~20% after 30 min	[58]
Ni-Bi/ $BiVO_4$	1.3 mA/cm <sup>2</sup>	100 mV	~30% after 3h	[19]
Co-Pi/W: $BiVO_4$	1.4 mA/cm <sup>2</sup>	440 mV	~45% after 2 h	[59]
Co-Bi/ $BiVO_4$	2.0 mA/cm <sup>2</sup>	320 mV	55% after 2.7h	[60]
FeOOH/ $BiVO_4$	2.2 mA/cm <sup>2</sup>	500 mV	2% after 6h	[61]
Co <sub>2</sub> N <sub>0.67</sub> / $BiVO_4$	2.21 mA/cm <sup>2</sup>	200 mV	40% after 10 min	[62]
IrCOOH/ $BiVO_4$	2.8 mA/cm <sup>2</sup>	400 mV	Near zero in 100 s	[63]
AgO <sub>x</sub> /NiO <sub>x</sub> / $BiVO_4$	2.25 mA/cm <sup>2</sup>	270 mV	11% for 4h	[64]
NiFe-LDH/ $BiVO_4$	1.21 mA/cm <sup>2</sup>	320 mV	10% after 12 h	[20]
FeOOH/NiOOH/ $BiVO_4$	4.2 mA/cm <sup>2</sup>	120 mV	No decay in 48h	[46]

demonstrated that the presence of a phosphate group plays a critical role in stabilizing the metal catalytic active centers, thereby facilitating the oxidation of water [55,56]. Hence, the presence of Fe-Pi effectively facilitated the hole transfer from BVO to the electrolyte and improved the overall PEC performance by suppressing the recombination. Generally, the function of the Fe-Pi co-catalyst is to tune the balance between charge transfer kinetics and surface charge recombination.

Based on the above discussions, it is reasonable to confer that BVO surface modification by Fe-Pi can be a beneficial method for enhancing the surface charge collection efficiency of the BVO photoanode. This modification of BVO provides an alternative pathway for water oxidation that diminishes the hole accumulation at the BVO surface. Therefore, the large PEC water splitting overpotential of BVO caused by

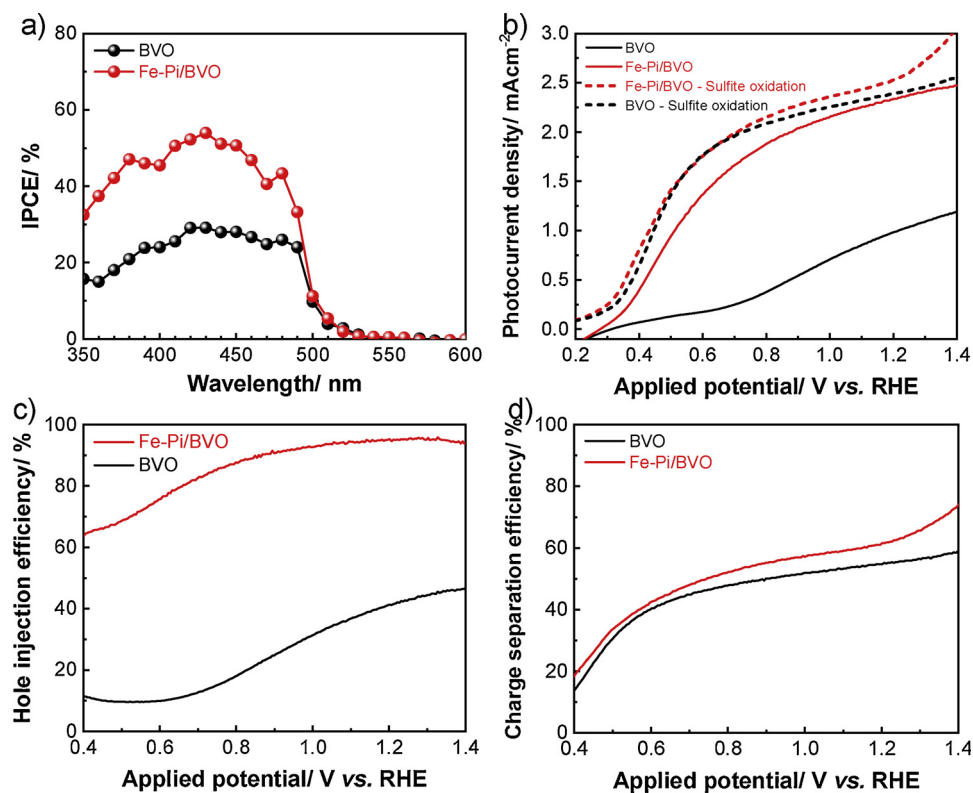


Fig. 7. IPCE measured at 1.23 V vs. the RHE under monochromatic light irradiation of BVO and Fe-Pi/BVO (a); J-V curve for sulfite oxidation (b); surface charge transfer efficiency (c) and bulk charge separation efficiency (d) versus applied potential curve under illumination of BVO and Fe-Pi/BVO.

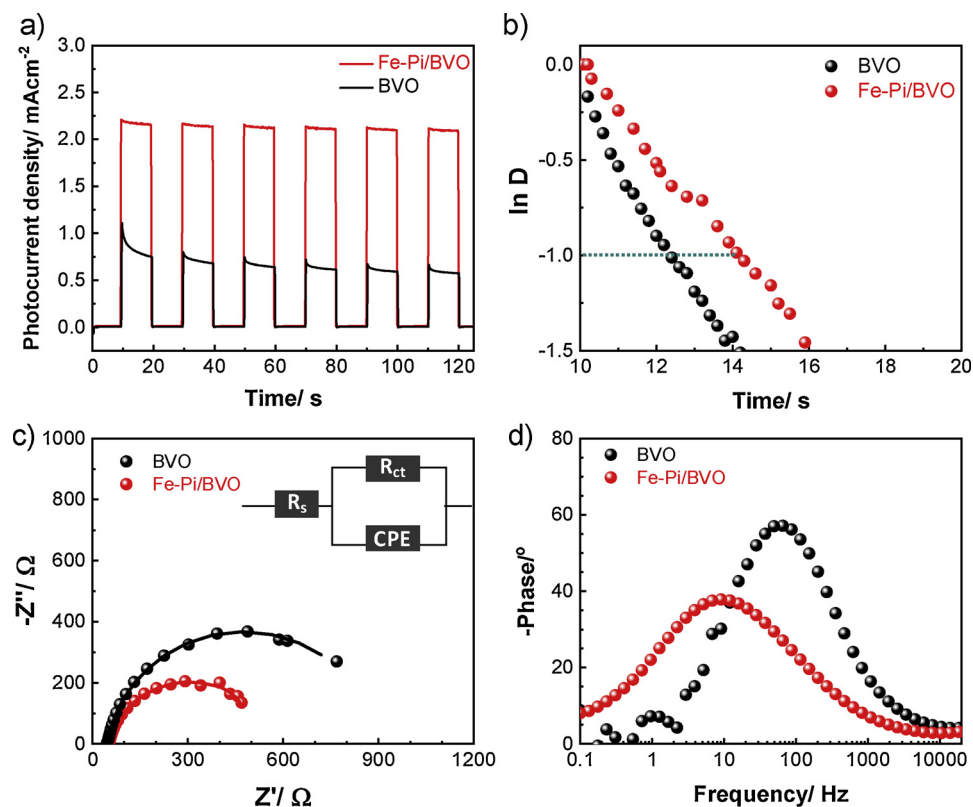


Fig. 8. Transient photocurrent density as a function of time (a); transient photocurrent decay time under illumination (b); Nyquist plot (c) and Bode plots (d) of BVO and Fe-Pi/BVO at 1.23 V versus RHE under illumination.



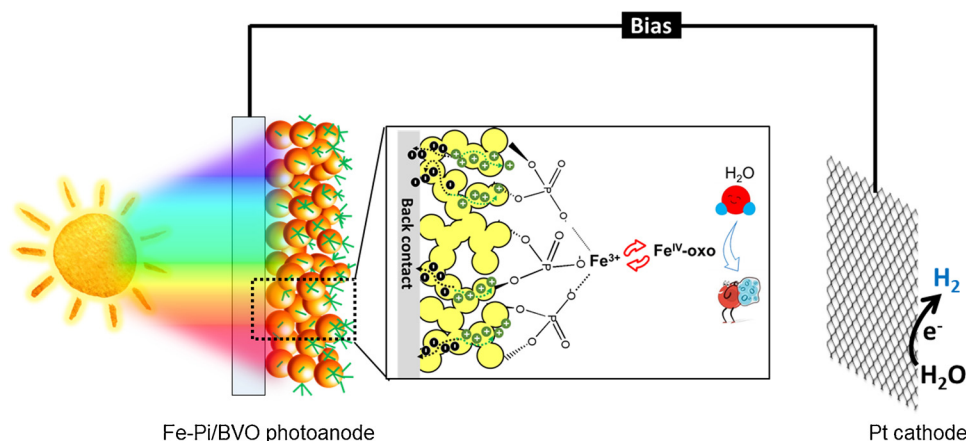


Fig. 9. Schematic illustration for water oxidation mechanism on Fe-Pi/BVO photoanode.

its poor kinetics can be significantly reduced.

#### 4. Conclusion

In this study, we successfully synthesized unique ferric phosphate nanosheet as an efficient oxygen evolution catalyst on the surface of a light absorber by using a facile, green and cost-efficient binderless SILAR method. The integrated photoanode is beneficial in that it reduces surface kinetics, boosts the photoelectrochemical water oxidation rate and shifts the water oxidation onset potential with ca. 500 mV in a negative direction, as well as improving long-term stability. The superior PEC behaviors benefit from the improved charge transfer efficiency caused by the coupling with ferrite phosphate, which provides an alternative pathway for the transfer of holes. More generally, this work emphasizes that composite photoanode strategies have significant potential for the development of sustainable, environmental, and efficient photoelectrodes for solar-driven water splitting, as well as mechanistic insights important for BVO, applied for efficient photoelectrochemical water splitting.

#### Acknowledgments

This work was financially supported from the Young Scholar Fellowship Program by Ministry of Science and Technology (MOST) in Taiwan, under Grant MOST107-2636-E-011-001. The authors would like to express their gratitude to National Taiwan University of Science and Technology for facilities support.

#### Appendix A. Supplementary data

Supplementary material related to this article can be found, in the online version, at doi:<https://doi.org/10.1016/j.apcatb.2018.11.001>.

#### References

- [1] J. Zhou, A. Zhou, L. Shu, M.-C. Liu, Y. Dou, J.-R. Li, Cellular heterojunctions fabricated through the sulfurization of MOFs onto ZnO for high-efficient photoelectrochemical water oxidation, *Appl. Catal. B Environ.* 226 (2018) 421–428.
- [2] F.M. Toma, J.K. Cooper, V. Kunzelmann, M.T. McDowell, J. Yu, D.M. Larson, N.J. Borys, C. Abelyan, J.W. Beeman, K.M. Yu, J. Yang, L. Chen, M.R.S.J. Spurgeon, F.A. Houle, K.A. Persson, I.D. Sharp, Mechanistic insights into chemical and photochemical transformations of bismuth vanadate photoanodes, *Nat. Commun.* 7 (2016) 12012.
- [3] F.F. Abdi, T.J. Savenije, M.M. May, B. Dam, R. Van De Krol, The origin of slow carrier transport in BiVO<sub>4</sub> thin film photoanodes: a time-resolved microwave conductivity study, *J. Phys. Chem. Lett.* 4 (2013) 2752–2757.
- [4] J. Eichhorn, J. Christoph Kastl, D.K. Cooper, A.M. Ziegler, I.D. Schwartzberg, S. Toma, F.M. Toma, Nanoscale imaging of charge carrier transport in water splitting photoanodes, *Nat. Commun.* 8 (2018) 2597.
- [5] Y. Ma, S.R. Pendlebury, A. Reynal, F. Le Formal, J.R. Durrant, Dynamics of photogenerated holes in undoped BiVO<sub>4</sub> photoanodes for solar water oxidation, *Chem. Sci.* 5 (2014) 2964–2973.
- [6] Y. Pihosh, I. Turkevych, K. Mawatari, J. Uemura, Y. Kazoe, S. Kosar, K. Makita, T. Sugaya, T. Matsui, D. Fujita, M. Tosa, M. Kondo, T. Kitamori, Photocatalytic generation of hydrogen by core-shell WO<sub>3</sub>/BiVO<sub>4</sub> nanorods with ultimate water splitting efficiency, *Sci. Rep.* 5 (2015) 11141.
- [7] B. Lamm, B.J. Trzeźniewski, H. Döschner, W.A. Smith, M. Stefik, Emerging post-synthetic improvements of BiVO<sub>4</sub> photoanodes for solar water splitting, *ACS Energy Lett.* 3 (2018) 112–124.
- [8] M.-W. Kim, E. Samuel, K. Kim, H. Yoon, B. Joshi, M.T. Swihart, S.S. Yoon, Tuning the morphology of electrosprayed BiVO<sub>4</sub> from nanopillars to nanoferns via pH control for solar water splitting, *J. Alloys Compd.* 769 (2018) 193–200.
- [9] B. Zhang, H. Zhang, Z. Wang, X. Zhang, X. Qin, Y. Dai, Y. Liu, P. Wang, Y. Li, B. Huang, Doping strategy to promote the charge separation in BiVO<sub>4</sub> photoanodes, *Appl. Catal. B Environ.* 211 (2017) 258–265.
- [10] J.A. Seabold, K. Zhu, N.R. Neale, Efficient solar photoelectrolysis by nanoporous Mo: BiVO<sub>4</sub> through controlled electron transport, *Phys. Chem. Chem. Phys.* 16 (2014) 1121–1131.
- [11] Y. Bu, J. Tian, Z. Chen, Q. Zhang, W. Li, F.H. Tian, J.P. Ao, Optimization of the photo-electrochemical performance of Mo-doped BiVO<sub>4</sub> photoanode by controlling the metal-oxygen bond state on (020) facet, *Adv. Mater. Interfaces* 4 (2017) 1–9.
- [12] S.M. Thalluri, S. Hernández, S. Bensaid, G. Saracco, N. Russo, Green-synthesized W- and Mo-doped BiVO<sub>4</sub> oriented along the {040} facet with enhanced activity for the sun-driven water oxidation, *Appl. Catal. B Environ.* 180 (2016) 630–636.
- [13] L. Qian, C. Wang, A. Chen, H. Yang, BiOI nanosheets grown by chemical vapor deposition and its conversion to highly efficient BiVO<sub>4</sub> photoanode, *Chinese J. Chem.* 35 (2017) 30–34.
- [14] L. Deng, S. Jingying, L. Can, Transition-metal-based electrocatalysts as cocatalysts for photoelectrochemical water splitting: a mini review, *Small* 14 (2018) 1704179.
- [15] Y. Bi, B. Zhang, L. Wang, Y. Zhang, Y. Ding, Ultrathin FeOOH nanolayers with rich oxygen vacancies on BiVO<sub>4</sub> photoanodes for efficient water oxidation, *Angew. Chemie Int. Ed.* (2018) 1–6.
- [16] B.M. Hunter, H.B. Gray, A.M. Müller, Earth-abundant heterogeneous water oxidation catalysts, *Chem. Rev.* 116 (2016) 14120–14136.
- [17] F.S. Hegner, I. Herranz-Cardona, D. Cardenas-Morcoso, N. López, J.-R. Galán-Mascarós, S. Gimenez, Cobalt hexacyanoferrate on BiVO<sub>4</sub> photoanodes for robust water splitting, *Appl. Mater. Interfaces* 9 (2017) 37671–37681.
- [18] M.F. Lichterman, M.R. Shaner, S.G. Handler, B.S. Brunschwig, H.B. Gray, N.S. Lewis, J.M. Spurgeon, Enhanced stability and activity for water oxidation in alkaline media with bismuth vanadate photoelectrodes modified with a cobalt oxide catalytic layer produced by atomic layer deposition, *J. Phys. Chem. Lett.* 4 (2013) 4188–4191.
- [19] S.K. Choi, W. Choi, H. Park, Solar water oxidation using nickel-borate coupled BiVO<sub>4</sub> photoelectrodes, *Phys. Chem. Chem. Phys.* 15 (2013) 6499–6507.
- [20] Y. Zhu, J. Ren, X. Yang, G. Chang, Y. Bu, G. Wei, W. Han, D. Yang, Interface engineering of 3D BiVO<sub>4</sub>/Fe-based layered double hydroxide core/shell nanostructures for boosting photoelectrochemical water oxidation, *J. Mater. Chem. A* 7 (2017) 9952–9959.
- [21] B.E. Wu, C.Y. Chiang, Photochemical metal organic deposition of FeO<sub>x</sub> catalyst on BiVO<sub>4</sub> for improving solar-driven water oxidation efficiency, *J. Taiwan Inst. Chem. Eng.* 80 (2017) 1014–1021.
- [22] S.K. Pilli, T.E. Furtak, L.D. Brown, T.G. Deutsch, J.A. Turner, A.M. Herring, Cobalt-phosphate (Co-Pi) catalyst modified Mo-doped BiVO<sub>4</sub> photoelectrodes for solar water oxidation, *Energy Environ. Sci.* 4 5028 (2011).
- [23] X. Zhao, C. Zhou, B. Han, Z. Ji, L. Wang, J. Wu, Growth mechanism of curved Mg-Al-CO<sub>3</sub> layered double hydroxide nanostructures in a one-pot assembly procedure under ambient pressure, *RSC Adv.* 5 (2015) 19955–19960.
- [24] K. Dang, X. Chang, T. Wang, J. Gong, Enhancement of photoelectrochemical oxidation by an amorphous nickel boride catalyst on porous BiVO<sub>4</sub>, *Nanoscale* 9 (2017) 16133–16137.
- [25] T. Palaniselvam, L. Shi, G. Mettela, D.H. Anjum, R. Li, K.P. Katuri, P.E. Saikaly, P. Wang, Vastly enhanced BiVO<sub>4</sub> photocatalytic OER performance by NiCoO<sub>4</sub> as cocatalyst, *Adv. Mater. Interfaces* 1700540 (2017) 1–10.

- [26] Y. Li, C. Zhao, Iron-doped nickel phosphate as synergistic electrocatalyst for water oxidation, *Chem. Mater.* 28 (2016) 5659–5666.
- [27] B. Klahr, S. Gimenez, F. Fabregat-Santiago, J. Bisquert, T.W. Hamann, Photoelectrochemical and impedance spectroscopic investigation of water oxidation with “Co-Pi”-coated hematite electrodes, *J. Am. Chem. Soc.* 134 (2012) 16693–16700.
- [28] K. Jin, J. Park, J. Lee, K.D. Yang, G.K. Pradhan, U. Sim, D. Jeong, H.L. Jang, S. Park, D. Kim, N.-E. Sung, S.H. Kim, S. Han, K.T. Nam, Hydrated manganese (II) phosphate ( $\text{Mn}_3(\text{PO}_4)_2 \cdot 3\text{H}_2\text{O}$ ) as a water oxidation catalyst, *J. Am. Chem. Soc.* 136 (2014) 7435–7443.
- [29] A. Vasileff, S. Chen, S.Z. Qiao, Three dimensional nitrogen-doped graphene hydrogels with in situ deposited cobalt phosphate nanoclusters for efficient oxygen evolution in a neutral electrolyte, *Nanoscale Horiz.* 1 (2016) 41–44.
- [30] L. Xie, R. Zhang, L. Cui, D. Liu, S. Hao, Y. Ma, G. Du, A.M. Asiri, X. Sun, High-performance electrolytic oxygen evolution in neutral media catalyzed by a cobalt phosphate nanorod array, *Angew. Chemie - Int. Ed.* 56 (2017) 1064–1068.
- [31] D. Yin, Z. Jin, M. Liu, T. Gao, H. Yuan, D. Xiao, Microwave-assisted synthesis of the cobalt-iron phosphates nanosheets as an efficient electrocatalyst for water oxidation, *Electrochim. Acta* 260 (2018) 420–429.
- [32] B. Liu, H.-Q. Peng, C.-N. Ho, H. Xue, S. Wu, T.-W. Ng, C.-S. Lee, W. Zhang, mesoporous nanosheet networked hybrids of cobalt oxide and cobalt phosphate for efficient electrochemical and photoelectrochemical oxygen evolution, *Small* 13 (2017) 1701875.
- [33] J. Gan, B.B. Rajeeva, Z. Wu, D. Penley, C. Liang, Y. Tong, Y. Zheng, Plasmon-enhanced nanoporous  $\text{BiVO}_4$  photoanodes for efficient photoelectrochemical water oxidation, *Nanotechnology* 27 (2016) 235401.
- [34] J. Gan, X. Lu, B.B. Rajeeva, R. Menz, Y. Tong, Y. Zheng, Efficient photoelectrochemical water oxidation over hydrogen-reduced nanoporous  $\text{BiVO}_4$  with Ni-Bi electrocatalyst, *ChemElectroChem* 2 (2015) 1385–1395.
- [35] D. Zhong, L. Liu, D. Li, C. Wei, Q. Wang, G. Hao, Q. Zhao, J. Li, Facile and fast fabrication of iron-phosphate supported on nickel foam as a highly efficient and stable oxygen evolution catalyst, *J. Mater. Chem. A* 5 (2017) 18627–18633.
- [36] P. Luan, M. Xie, X. Fu, Y. Qu, X. Sun, L. Jing, Improved photoactivity of  $\text{TiO}_2$ -Fe $_2\text{O}_3$  nanocomposites for visible-light water splitting after phosphate bridging and its mechanism, *Phys. Chem. Chem. Phys.* 17 (2015) 5043–5050, <https://doi.org/10.1039/C4CP04631E>.
- [37] L. Jing, J. Zhou, J.R. Durrant, J. Tang, D. Liu, H. Fu, Dynamics of photogenerated charges in the phosphate modified  $\text{TiO}_2$  and the enhanced activity for photoelectrochemical water splitting, *Energy Environ. Sci.* 5 (2012) 6552–6558.
- [38] K.J.A. Raj, A.V. Ramaswamy, B. Viswanathan, Surface area, pore size, and particle size engineering of titania with seeding technique and phosphate modification, *J. Phys. Chem. C* 113 (2009) 13750–13757.
- [39] N. Guijarro, M.S. Prévot, X. Yu, X.A. Jeanbourquin, P. Bornoz, W. Bourée, M. Johnson, F. Le Formal, K. Sivula, A bottom-up approach toward all-solution-processed high-efficiency  $\text{Cu}(\text{In,Ga})\text{S}_2$  photocathodes for solar water splitting, *Adv. Energy Mater.* 6 (2016) 1501949.
- [40] D.K. Zhong, M. Cornuz, K. Sivula, M. Grätzel, D.R. Gamelin, Photo-assisted electrodeposition of cobalt-phosphate (Co-Pi) catalyst on hematite photoanodes for solar water oxidation, *Energy Environ. Sci.* 4 (2011) 1759.
- [41] M. Barroso, A.J. Cowan, S.R. Pendlebury, M. Grätzel, D.R. Klug, J.R. Durrant, The role of cobalt phosphate in enhancing the photocatalytic activity of  $\alpha\text{-Fe}_2\text{O}_3$  toward water oxidation, *J. Am. Chem. Soc.* 133 (2011) 14868–14871.
- [42] W. Luo, Z. Yang, Z. Li, J. Zhang, J. Liu, Z. Zhao, Z. Wang, S. Yan, T. Yu, Z. Zou, Solar hydrogen generation from seawater with a modified  $\text{BiVO}_4$  photoanode, *Energy Environ. Sci.* 4 (2011) 4046–4051.
- [43] S.K. Pilli, T.G. Deutsch, T.E. Furtak, J.A. Turner, L.D. Brown, A.M. Herring, Light induced water oxidation on cobalt-phosphate (Co-Pi) catalyst modified semi-transparent, porous  $\text{SiO}_2$ - $\text{BiVO}_4$  electrodes, *Phys. Chem. Chem. Phys.* 14 (2012) 7032–7039.
- [44] D.K. Lee, K.-S. Choi, Enhancing long-term photostability of  $\text{BiVO}_4$  photoanodes for solar water splitting by tuning electrolyte composition, *Nat. Energy* 3 (2017) 53–60.
- [45] H. Dotan, K. Sivula, M. Grätzel, A. Rothschild, S.C. Warren, Probing the photoelectrochemical properties of hematite  $\text{Fe}_2\text{O}_3$  electrodes using hydrogen peroxide as a hole scavenger, *Energy Environ. Sci.* 4 (2011) 958–964.
- [46] T.W. Kim, K.-S. Choi, Nanoporous  $\text{BiVO}_4$  photoanodes with dual-layer oxygen evolution catalysts for solar water splitting, *Science* (80-) 343 (2014) 990–994.
- [47] T.-G. Vo, J.-M. Chiu, Y. Tai, C.-Y. Chiang, Turnip-inspired  $\text{BiVO}_4$ /CuSCN nanostructure with close to 100% suppression of surface recombination for solar water splitting, *Sol. Energy Mater. Sol. Cells* 185 (2018) 415–424.
- [48] G. Lili, L. Feng, H. Haiguo, L. Xuefeng, X. Na, H. Yiping, W. Shenqi, W. Chenglong, M. Jiantai, J. Jun, Dual modification of  $\text{BiVO}_4$  photoanode by constructing heterojunction with  $\text{NiMoO}_4$  and depositing CoPi co-catalyst for enhanced photoelectrochemical performance, *ChemSusChem* 11 (2018) 1–9.
- [49] X. An, C. Hu, H. Lan, H. Liu, J. Qu, Strongly coupled metal oxide/reassembled carbon nitride/Co-Pi heterostructures for efficient photoelectrochemical water splitting, *ACS Appl. Mater. Interfaces* 10 (2018) 6424–6432.
- [50] C. Panda, J. Debgupta, D. Díaz Díaz, K.K. Singh, S. Sen Gupta, B.B. Dhar, Homogeneous photochemical water oxidation by biuret-modified Fe-TAML: evidence of  $\text{Fe}(\text{V})$  intermediate, *J. Am. Chem. Soc.* 136 (2014) 12273–12282.
- [51] L.D. Wickramasinghe, R. Zhou, R. Zong, P. Vo, K.J. Gagnon, R.P. Thummel, Iron complexes of square planar tetradentate polypyridyl-type ligands as catalysts for water oxidation, *J. Am. Chem. Soc.* 137 (2015) 13260–13263.
- [52] O. Zandi, T.W. Hamann, Determination of photoelectrochemical water oxidation intermediates on hematite electrode surfaces using operando infrared spectroscopy, *Nat. Chem.* 8 (2016) 778.
- [53] J. Liu, R. Zhu, T. Xu, Y. Xu, F. Ge, Y. Xi, J. Zhu, H. He, Co-adsorption of phosphate and zinc(II) on the surface of ferrihydrite, *Chemosphere* 144 (2016) 1148–1155.
- [54] L. Fu, H. Yu, C. Zhang, Z. Shao, B. Yi, Cobalt phosphate group modified hematite nanorod array as photoanode for efficient solar water splitting, *Electrochim. Acta* 136 (2014) 363–369.
- [55] Y. Zhan, M. Lu, S. Yang, C. Xu, Z. Liu, J.Y. Lee, Activity of transition-metal (manganese, iron, cobalt, and nickel) phosphates for oxygen electrocatalysis in alkaline solution, *ChemCatChem* 8 (2016) 372–379.
- [56] K. Jin, J. Park, J. Lee, K.D. Yang, G.K. Pradhan, U. Sim, D. Jeong, H.L. Jang, S. Park, D. Kim, N.-E. Sung, S.H. Kim, S. Han, K.T. Nam, Hydrated manganese(II) phosphate ( $\text{Mn}_3(\text{PO}_4)_2 \cdot 3\text{H}_2\text{O}$ ) as a water oxidation catalyst, *J. Am. Chem. Soc.* 136 (2014) 7435–7443.
- [57] S.K. Pilli, K. Summers, D. Chidambaram, Ni-Ci oxygen evolution catalyst integrated  $\text{BiVO}_4$  photoanodes for solar induced water oxidation, *RSC Adv.* 5 (2015) 47080–47089.
- [58] Y. Liang, J. Messinger, Improving  $\text{BiVO}_4$  photoanodes for solar water splitting through surface passivation, *Phys. Chem. Chem. Phys.* 16 (2014) 12014–12020.
- [59] D.K. Zhong, S. Choi, D.R. Gamelin, Near-complete suppression of surface recombination in solar photoelectrolysis by “Co-Pi” catalyst-modified  $\text{W:BiVO}_4$ , *J. Am. Chem. Soc.* 133 (2011) 18370–18377.
- [60] C. Ding, J. Shi, D. Wang, Z. Wang, N. Wang, G. Liu, F. Xiong, C. Li, Visible light driven overall water splitting using cocatalyst/ $\text{BiVO}_4$  photoanode with minimized bias, *Phys. Chem. Chem. Phys.* 15 (2013) 4589–4595.
- [61] J.A. Seabold, K.-S. Choi, Efficient and stable photo-oxidation of water by a Bismuth Vanadate photoanode coupled with an iron oxyhydroxide oxygen evolution catalyst, *J. Am. Chem. Soc.* 134 (2012) 2186–2192.
- [62] X. Wan, J. Su, L. Guo, Enhanced photoelectrochemical water oxidation on  $\text{BiVO}_4$  with mesoporous cobalt nitride sheets as oxygen-evolution cocatalysts, *Eur. J. Inorg. Chem.* 2018 (2018) 2557–2563.
- [63] M. Kan, D. Xue, A. Jia, X. Qian, D. Yue, J. Jia, Y. Zhao, A highly efficient nanoporous  $\text{BiVO}_4$  photoelectrode with enhanced interface charge transfer Co-catalyzed by molecular catalyst, *Appl. Catal. B Environ.* 225 (2018) 504–511.
- [64] Y. Hu, Y. Wu, J. Feng, H. Huang, C. Zhang, Q. Qian, T. Fang, J. Xu, P. Wang, Z. Li, Z. Zou, Rational design of electrocatalysts for simultaneously promoting bulk charge separation and surface charge transfer in solar water splitting photoelectrodes, *J. Mater. Chem. A* 6 (2018) 2568–2576.